JGR Solid Earth

RESEARCH ARTICLE
10.1029/2020JB020396

Key Points:
- Shipboard and satellite-derived bathymetry and gravity data differ by up to 1,600 m and 12 mGal, respectively, over seamounts in the northwest Pacific Ocean
- Bathymetry and gravity differences correlate closely and have been used to estimate the density of small-scale (<25 km wavelength) features on the seafloor
- Swath bathymetry data should always be acquired with gravity data for the constraints they provide on seamount internal structure, composition, and evolution

Correspondence to:
A. B. Watts,
tony.watts@earth.ox.ac.uk

Citation:
Watts, A. B., Tozer, B., Harper, H., Boston, B., Shillington, D. J., & Dunn, R. (2020). Evaluation of shipboard and satellite-derived bathymetry and gravity data over seamounts in the northwest Pacific Ocean. *Journal of Geophysical Research: Solid Earth*, *125*, e2020JB020396. https://doi.org/10.1029/2020JB020396

Received 11 JUN 2020
Accepted 23 SEP 2020
Accepted article online 25 SEP 2020

Evaluation of Shipboard and Satellite-Derived Bathymetry and Gravity Data Over Seamounts in the Northwest Pacific Ocean

A. B. Watts[1], B. Tozer[2], H. Harper[2], B. Boston[3], D. J. Shillington[4], and R. Dunn[5]

[1]Department of Earth Sciences, University of Oxford, Oxford, UK, [2]Scripps Institution of Oceanography, La Jolla, CA, USA, [3]Lamont-Doherty Earth Observatory, Columbia University, Palisades, NY, USA, [4]School of Earth and Sustainability, Northern Arizona University, Flagstaff, AZ, USA, [5]Department of Earth Sciences, School of Ocean and Earth Science and Technology, University of Hawaii, Honolulu, HI, USA

Abstract Earth's surface topography/bathymetry and gravity fields provide important constraints on crustal structure and the tectonic processes that act on it due, for example, to plate flexure and mantle convection. Such studies require, however, high accuracy measurements at a wide range of spatial scales. During the past few decades much progress has been made in the acquisition of bathymetry and gravity data using both shipboard and satellite altimeter methods. Surprisingly, there have been few comparisons of these data. During April–June, 2019 we had the opportunity onboard a R/V *Marcus G. Langseth* cruise in the northwest Pacific Ocean to compare data acquired with an EM122 Kongsberg swath bathymetry system and a refurbished Bell Aerospace BGM-3 gravimeter with the most recent global bathymetry and gravity fields. We find that while the recovery of bathymetry and gravity from satellite radar altimeter data in areas of sparse shipboard data has been impressive, root mean square discrepancies in the range 175.5–303.4 m and 2.6–6.3 mGal exist between shipboard and satellite-derived data. While these discrepancies are small, they are highly correlated and therefore have implications for the density structure, rock type and geological processes occurring on the deep seafloor. Shipboard data should continue to be acquired, especially over features such as seamounts, banks, and ridges that are associated with short wavelength (<25 km wavelength) bathymetric and gravimetric features beyond that is recoverable in satellite-derived data.

1. Introduction

Studies of Earth's bathymetry and gravity require accurate measurements at a wide range of spatial and temporal scales. Shipboard data have the advantage that it is acquired on the geoid and close to source, but the disadvantage of sparse coverage. Satellite data have the advantage of global coverage including areas where shipboard data are not available, but the disadvantage of limited resolution of small-scale features. Together though, shipboard and satellite bathymetry and gravity provide complimentary data sets which can be used as a critical constraint on the Earth's crust and mantle structure, processes, and evolution in water-covered regions.

Continuous shipboard bathymetry and gravity measurements have improved significantly since they were first acquired during World War II. The first bathymetry measurements using continuously recording single beam echo sounders were acquired in the 40s (e.g., Hess, 1946), and 3.5 kHz and 12 kHz precision depth recorders (PDRs) on academic research vessels have been in more or less continuous operation since then. In the late 70s (e.g., Renard & Allenou, 1979), an 11–12 kHz multibeam swath bathymetry system, SeaBeam, became available, and by the mid/late 80s similar hull-mounted transducer/receiver systems had been installed on a number of academic research vessels. It is now possible with modern systems such as the Kongsberg EM122 to measure seafloor depths to an accuracy of 1–2 m and to insonify the seafloor over widths as great as ~2.5 times the available water depth.

The first gravity measurements using continuously recording beam and vibrating-string type gravimeters mounted on gyro-stabilized platforms were introduced in the late 50s and early 60s (Tsuboi et al., 1961; Worzel, 1959). The accuracy of surface ship gravity measurements was initially limited by celestial navigation and dead reckoning, but the introduction of the U.S. Navy satellite navigation system in 1967 led to a significant reduction in cross-over errors at intersecting ship tracks (Talwani et al., 1966). It is now possible, for example, using modern versions of the Lacoste-Romberg air-sea and the Bell Aerospace BGM gravimeter together with GPS modern navigation to obtain an accuracy of 1–2 mGal and resolution of 2–10 km over the deep ocean, depending on sea state (Bell & Watts, 1986; Hildebrand et al., 1990). Moreover, the reporting of sub-mGal accuracies and higher resolution from some sea gravimeters (Casten & Haussmann, 1990) and gravity gradiometry (Bell et al., 1997), in which the full tensor field is measured, provide an exciting prospect for future work.

Similarly, satellite-derived bathymetry and gravity data have seen significant improvement since their early development following NASA's pioneering Geos-3 (Stanley, 1979) and SEASAT (Born et al., 1979) altimeter missions in the late 70s. Altimeters measure the distance between an orbiting satellite and the instantaneous sea surface, which in the absence of oceanographic "noise" can be used to calculate the gravimetric geoid and hence, from its slope, mean gravity anomalies (Lerch et al., 1982). As Dixon et al. (1983), Smith and Sandwell (1994), and Smith and Sandwell (1997) have shown, altimeter-derived gravity data can be used, together with a specially shaped reciprocal isostatic admittance function, to predict bathymetry in unsurveyed areas. It is now possible with altimeter data from satellites such as ERS-1, GeoSAT, CryoSat-2, Jason-1, Jason-2, and SARAL/AltiKa to recover bathymetry with a root mean square (RMS) misfit of ±180 m (Tozer et al., 2019) and gravity with a RMS misfit of 1–2 mGal (Sandwell et al., 2019) with respect to available shipboard measurements in the deep ocean. Significantly, larger errors, however, have been reported near shorelines (Widiwijayanti et al., 2003) and from regions of short wavelength bathymetry (Picard et al., 2017).

Curiously, there have been relatively few studies that have compared shipboard and satellite-derived bathymetry and gravity data. Smith and Sandwell (1994) compared an 1800-km-long transect of shipboard bathymetry data (R/V *Ewing* cruise 92-01) to satellite-derived data and found a RMS difference of 257 m and a coherence between the two fields down to wavelengths of ~30 km. More recently, Watts et al. (2006) compared shipboard and satellite-derived bathymetry data (V8.2) (Smith & Sandwell, 1997) at the Line islands and the Hawaiian ridge and found RMS differences of 466.5 and 467.7 m, respectively. Marks (1996) compared shipboard gravity data acquired along seven transits (up to 3,500 km long) onboard R/V *Shackleton*, *Discovery*, *Ewing* (cruise 92-01), *Moana Wave* and *Conrad* to the satellite-derived data of V7.2 (Smith & Sandwell, 1995) and found a RMS difference between the satellite-derived and shipboard gravity of 3–9 mGal and a coherence between the two fields down to wavelengths of 23–30 km. More recently, Ligi et al. (2012) compared shipboard and satellite derived gravity in the Red Sea and obtained differences up to 10 mGal, and Marks et al. (2013) found coherence between the two fields down to ~20 km.

The relationship between bathymetry and gravity has the potential to constrain density, rock type, and processes occurring on the seafloor. At long (>100 km) wavelengths bathymetric features are compensated and the relationship provides information on the state of isostasy, but at short (<100 km) wavelengths bathymetric features are essentially uncompensated (Watts & Moore, 2017) and can be used to extract mean water depth and density. Nettleton's method (Nettleton, 1939) in which the density is found that minimizes the correlation between topography and Bouguer gravity anomaly has long been used, for example, in the continents to profile density and infer rock type. In oceanic regions, the attenuation effects of water depth need to be considered. Kalnins and Watts (2009), for example, have used the relationship between bathymetry and gravity as a function of wavelength (i.e., admittance) to recover density in the West Pacific Ocean, finding a median of 2,598 kg m^{-3} and a peak in the range 2,700–2,800 kg m^{-3}. In 80% of their analysis windows, Kalnins and Watts (2009) found densities in the range 2,000–3,000 kg m^{-3}, comparable to the density range (2,300–2,900 kg m^{-3}) measured by Carlson and Raskin (1984) from samples and downhole logs in igneous basement at Deep Sea Drilling Project sites and partly attributed by them to spatial variations in porosity. Bathymetry and gravity data therefore have the potential for remotely sensing the physical properties of rocks on the seabed.

During April–May 2019, we had the opportunity onboard the Lamont-Doherty Earth Observatory of Columbia University operated R/V *Marcus G. Langseth* to compare bathymetry data acquired with a Kongsberg EM 122 swath bathymetry system, a recently refurbished BGM-3 gravimeter and GPS (modern) with the most recent versions of global satellite-derived bathymetry and gravity fields in the northwest Pacific Ocean. The cruise focus was on the Musician Seamounts and Emperor Seamount Chain where previous shipboard swath bathymetry and gravity anomaly data are sparse. We found that while the recovery of

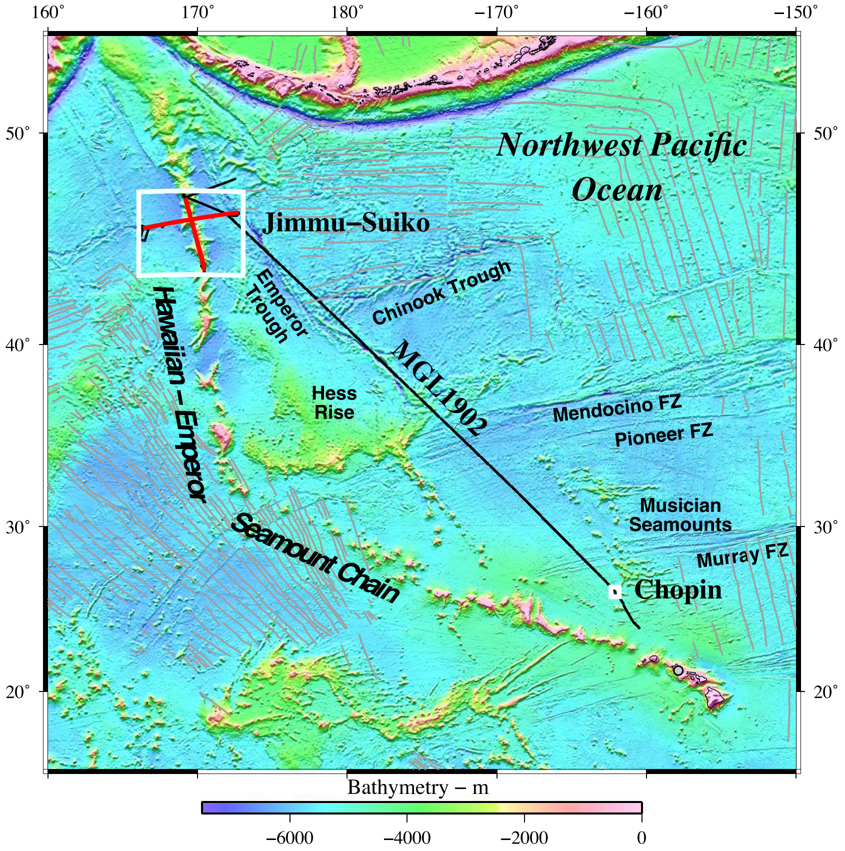

Figure 1. Location of MGL1902 ship tracks in the Northwest Pacific Ocean. Solid black and red lines show ship tracks. White outline boxes show the Chopin, and the Jimmu and Suiko seamount survey areas where coincident swath bathymetry and gravity anomaly data were acquired. Free-air gravity anomaly data within the two survey areas and along the transit between them were used to construct the power spectra in Figure 2a. The bathymetry/topography map is from SRTM15 + V2.0 (Tozer et al., 2019), and the magnetic lineations (light gray solid lines), which reflect the tectonic fabric of the seafloor, are based on Cande et al. (1989). The map shows that the MGL1902 ship tracks are almost entirely confined to the Cretaceous "quiet" zone (~118–83 Ma) when Earth's magnetic field did not reverse polarity.

satellite-derived bathymetry and gravity has been impressive, discrepancies of up to several mGal and hundreds of meters remain between surface ship measurements and the most recent satellite-derived fields. These discrepancies may seem small, but they have significant implications for interpretation of geological processes and, for example, the structure and composition of oceanic crust, the internal structure of seamounts, and deep-water sedimentation. Shipboard gravity measurements will therefore still be required in the future in order to determine the full form of the gravity and bathymetry field, especially over features such as seamounts where the bathymetry and its associated gravity anomaly has a significant short wavelength component that cannot be recovered by satellite data.

2. Bathymetry and Gravity Data

2.1. Shipboard Measurements

The shipboard bathymetry and gravity data used in this study were acquired during cruise MGL1902 of R/V *Marcus G. Langseth* from Honolulu (Hawai'i) to Kodiak (Alaska) in the northwest Pacific Ocean (Figure 1). The cruise included a 3,947-km-long transit between the Hawaiian Ridge and Emperor Seamounts, a sonar test over Chopin in the Musician Seamounts and a deep seismic survey of Jimmu and Suiko in the Emperor Seamounts.

The multibeam swath system, which has been operated on *Langseth* since the vessel underwent a major refurbishment in 2006, comprises 432 beams athwartships per ping, transmitting at a frequency of 12.0 kHz with maximum possible angular coverage of 150°. During MGL1902, the system was set with an angular swath width of 108° to 136° in an equal area mode (not equal angle), where the beam former projects beams of varying angle across the swath to create equal size sonar footprints on the seafloor, resulting in a footprint of roughly 20 m in 2,500 m of water. All swath bathymetry data acquired during MGL1902 were manually edited with the MB-System (Caress & Chayes, 2019) algorithms. The ping rate was ~1–2 s in 1,900 m of water, and survey lines were collected at ~4.5–5.0 knots during the Chopin sonar test, ~4–4.5 knots during seismic data acquisition, and ~8–10 knots during Ocean Bottom Seismometer (OBS) deployments and recoveries. Maximum beam angles were generally set to 54° for both port and starboard sides since the outermost beams only recorded noise for larger apertures in deep water. At this beam angle, the swath width is ~2.75 times the available water depth. In shallow water, the beam angle was occasionally increased to 65° or even 75°. Sound velocity profiles were acquired throughout the main survey areas and used to convert ping travel times to seafloor depth.

The BGM-3 gravimeter (Bell & Watts, 1986), which was purchased by Lamont-Doherty Geological Observatory in 1984 and previously operated on R/V *Robert D. Conrad* and R/V *Ewing* and as a portable instrument on smaller vessels and aircraft, was also installed on R/V *Marcus G. Langseth* in 2006. The original BGM-3 gravimeter system included a data handling system in which the digital pulse rate from the sensor was electronically damped using a resistor-capacitor circuit (RC filter), converted to mGal, and corrected for Eotvos and Latitude (Bell & Watts, 1986). Subsequently, the data handling system was removed, and the uncorrected sensor digital pulse rate count is now logged directly onboard *Langseth* at 1 s interval. In June 2018, the sensor was replaced and the instrument recalibrated with a new pulse rate count to mGal conversion factor of 5.096606269 mGal/count and bias of 852,513.49 mGal using tie-in data between the BGM-3 gravimeter and the Honolulu Alpha absolute gravity station. Tie-in data since June 2018 indicate that the new sensor system has performed well with a small drift rate during MGL1902 of ~0.0744 mGal/day (Appendix A).

The tightly constrained BGM-3 sensor records only vertical accelerations, and so some form of filtering is required in order to separate Earth's gravity from the much larger accelerations that act on it due to ship motion. The latter can amount to hundreds of thousands of mGal, but the motion is periodic and so can, in principal, be removed by time or distance filtering.

2.2. Satellite-Derived Measurements

The satellite-derived fields used in this study are based mainly on the SRTM15 + V2.0 15 × 15 arc sec bathymetry grid of Tozer et al. (2019) and the V28.1 1 × 1 min free-air gravity anomaly grid of Sandwell et al. (2019). These fields are among the highest resolution global grids available to date. The bathymetry grid combines legacy shipboard single beam and multibeam swath bathymetry with predicted bathymetry from satellite-derived gravity data. Predicted bathymetry is estimated to have a root mean square (RMS) error of ±150 m in deep oceans and ±180 m in shallow coastal regions (Tozer et al., 2019). The V28.1 gravity grid is based on ERS-1 and GEOSAT and, since 2010, data derived from the CryoSat-2, Jason-1, Jason-2, and SARAL/AltiKa satellite altimeter missions. Satellite gravity is estimated to be accurate to ~1–2 mGal (Sandwell et al., 2019).

We have also considered other global grids such as GEBCO 2019 and 2020 (GEBCO Compilation Group, 2020) 15 × 15 arc sec bathymetry and DTU10 and DTU15 (Andersen et al., 2010, 2017) 1 × 1 min free-air gravity anomaly grids. GEBCO 2019 uses the predicted bathymetry from SRTM15 PLUS (V1) (Olson et al., 2014) as its base layer while GEBCO 2020 uses the predicted bathymetry from SRTM15 + V2.0 (Tozer et al., 2019) as its base layer and so we have not used this grid here as we found it identical to the final SRTM15 + V2.0 grid in the Chopin and Emperor seamount regions. DTU10 is a satellite-derived grid based on ERS-1 and GEOSAT and GFO ERM satellite altimeter missions. DTU15 is an updated grid that includes CryoSat-2, Jason-1, and SARAL/AltiKa mission data (Andersen et al., 2017).

3. Power Spectra

In order to process the shipboard MGL1902 gravity data, we first prepared a raw 1 s data file by converting the BGM-3 pulse rate count data to mGal, adding the bias and then applying corrections for Eötvös and Latitude. The raw data acquired in the two main survey areas and along the connecting transit were then used to calculate power spectra.

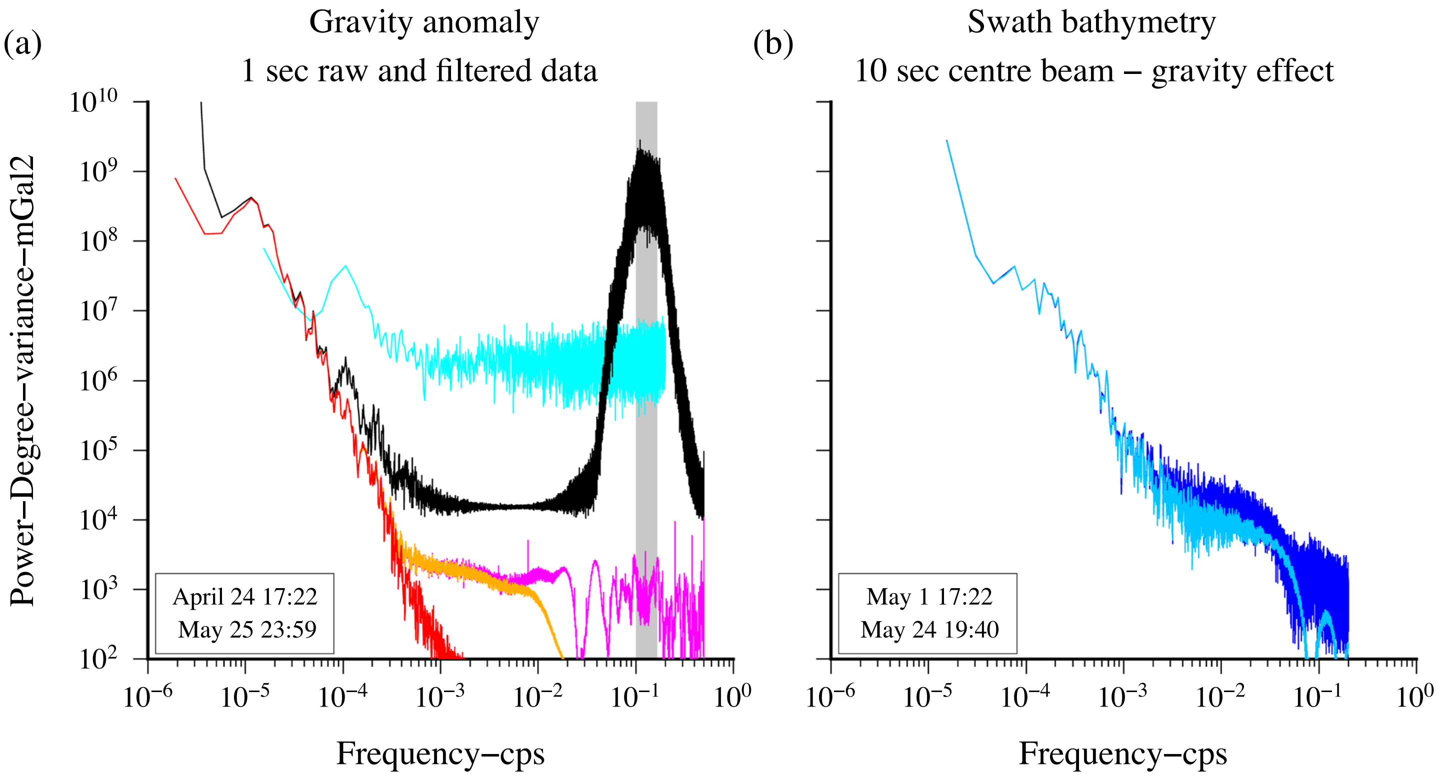

Figure 2. Power spectra plot of the shipboard gravity data acquired during MGL1902. (a) Observed BGM-3 shipboard gravity data. Solid black line: raw 1 s pulse rate data, which has been converted to mGal and had a bias added. Solid light blue line = raw 1 s free-air gravity anomaly data with a 10 s straight average applied before correcting for latitude and Eötvös. Solid magenta line: raw 1 s free-air gravity anomaly data with a 120 s Gaussian filter applied before correcting for latitude and Eötvös. Solid orange line: raw 1 s free-air gravity anomaly data with a 120 s Gaussian filter and a 0.3 km Gaussian filter. Solid red line: raw 1 s free-air gravity anomaly data with a 120 s Gaussian filter and a 1.0 km median filter. Gray shaded region shows frequency range of a 7-day-long record of virtual wave buoy data from the Jimmu and Suiko seamount survey area (Figure 1). (b) Calculated gravity effect of uncompensated bathymetry assuming the center beam swath bathymetry, the simple Bouguer "slab" formula and a density of seawater and oceanic crust of 1,030 and 2,650 kg m^{-3}, respectively. Solid blue line: raw 10 s swath data. Solid light blue line: raw 10 s swath data with a 2.0 km median filter.

Figure 2a shows the power spectra of the raw converted 1 s BGM-3 data (solid black line). The data range from a minimum of 90,981.40 mGal to a maximum of 1,137,301.8 mGal with an average of 980,472.0 mGal, the expected theoretical value at a latitude of 43.4°N. At low frequencies (long periods), the raw 1 s data spectra decrease with increase in frequency. This is the expected behavior of the gravitational field and reflects, in part, Earth's topography and bathymetry and its isostatic compensation (Kaula, 1967; Rapp, 1989; Watts & Moore, 2017). Spectra flatten at intermediate frequencies, rise abruptly to peak at high frequencies (short periods) of ~0.15 cps, and then fall rapidly. We attribute this peak to swell "noise," as is evidenced, for example, by virtual wave buoy data at latitude 47.8°N, longitude 163.5°E (NOAA, 2019), which recorded average swell periods of 6–10 s, sea heights of 2–3 m, and wind speeds of 12–16 knots during a 7-day-long period of the Emperor Seamount survey.

The swath bathymetry center beam data are currently logged on *Langseth* as a 10 s straight average so we first evaluated whether such an average might be suitable for filtering the gravity data. Figure 2a shows that a 10 s straight average (light blue curve) applied before correcting for latitude and Eötvös fails to eliminate swell "noise." The figure shows that a 120 s Gaussian filter (magenta curve), as recommended by the manufacturer, to be a much more satisfactory way of removing swell noise. A problem with this filter, however, is that there is still a significant level of noise at high frequencies (short periods), albeit with much less power than swell "noise." During the long transit between survey areas, the vessel made good an average speed of 8.9 knots and so in 120 s would have traveled an average of 0.5 km. We therefore considered applying an additional distance filtering step. We found that a 0.3 km Gaussian filter or a 1.0 km median filter further

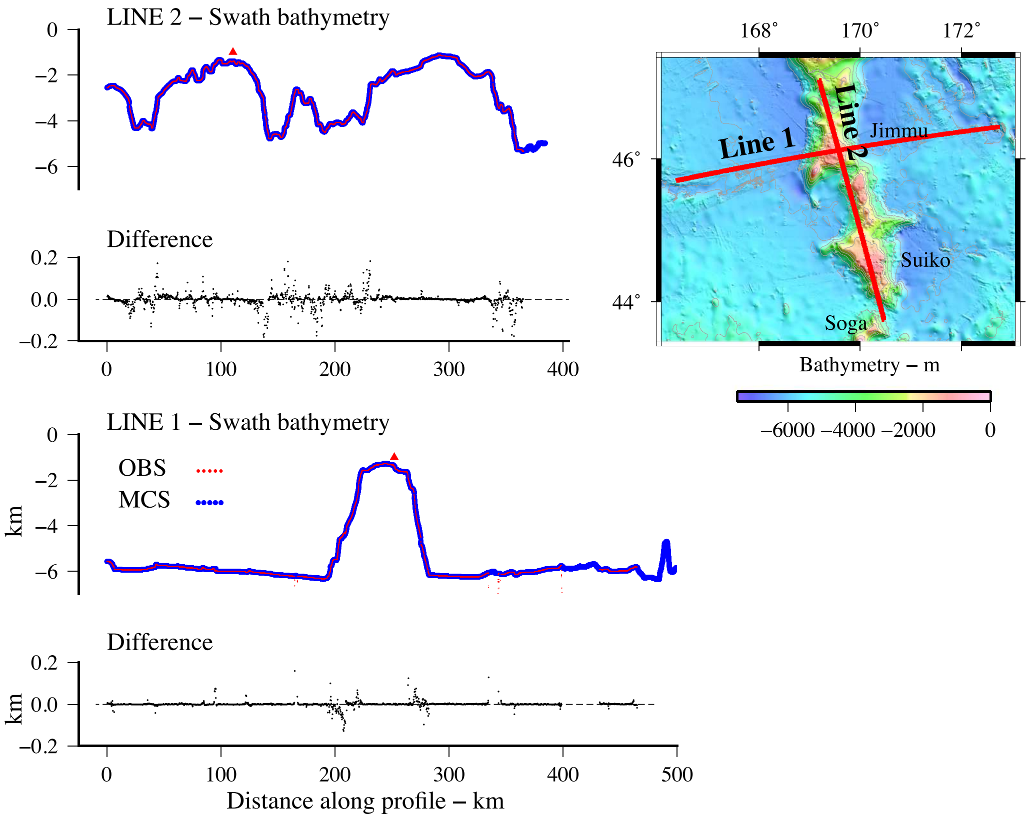

Figure 3. Comparison of swath bathymetry center beam data along repeat Lines 1 and 2 of Jimmu and Suiko seamounts. The raw 10 s data have been despiked with a 2.0 km median filter. Red filled triangle marks the intersection point of Lines 1 and 2. The difference plot shows the swath data acquired during MCS acquisition minus the swath data acquired during OBS acquisition. Only differences in the range −0.2 to 0.2 km are plotted.

reduced the noise at high frequencies (short periods), with the latter being particularly successful in extending the decrease in power with increasing frequency seen at low frequencies.

4. Repeat Swath Bathymetry and Gravity Measurements

We were fortunate during the deep seismic part of the survey to acquire two, 350- and 400-km long, repeat lines: once for multi-channel seismic (MCS) data and once for OBS data acquisition. Although these were not truly repeat lines (since the track of OBS shooting was offset slightly [~500 m] from the track of MCS shooting), we have been able to use the repeat lines to assess the accuracy (i.e., repeatability) of the shipboard bathymetry and gravity measurements on different track headings and in variable sea states.

Data acquired along the MCS and OBS repeat dip Line 1 and repeat strike Line 2 are shown in Figures 3 and 4. Swath bathymetry agrees well, with the main differences being confined to steep bathymetric gradients on the flanks of seamounts. RMS differences are greater for Line 2 than Line 1, probably because of the greater incidence on the strike line than the dip line of steep gradients. Gravity also agrees well. RMS differences are also greater for Line 2 than Line 1. Steep gradients on this line probably contribute, but navigational errors due, for example, to the sensitivity of heading changes to N-S courses in the Eötvös correction probably also contribute. Statistical data from the repeat lines are summarized in Table 1.

5. Comparison of Shipboard and Satellite-Derived Bathymetry and Gravity Data

5.1. Chopin, Musician Seamounts

Chopin Seamount is one of a number of elongate-shaped seamounts and east-west trending linear ridges that comprise the Musician Seamounts, north of the Hawaiian Ridge in the Central Pacific Ocean. Marine

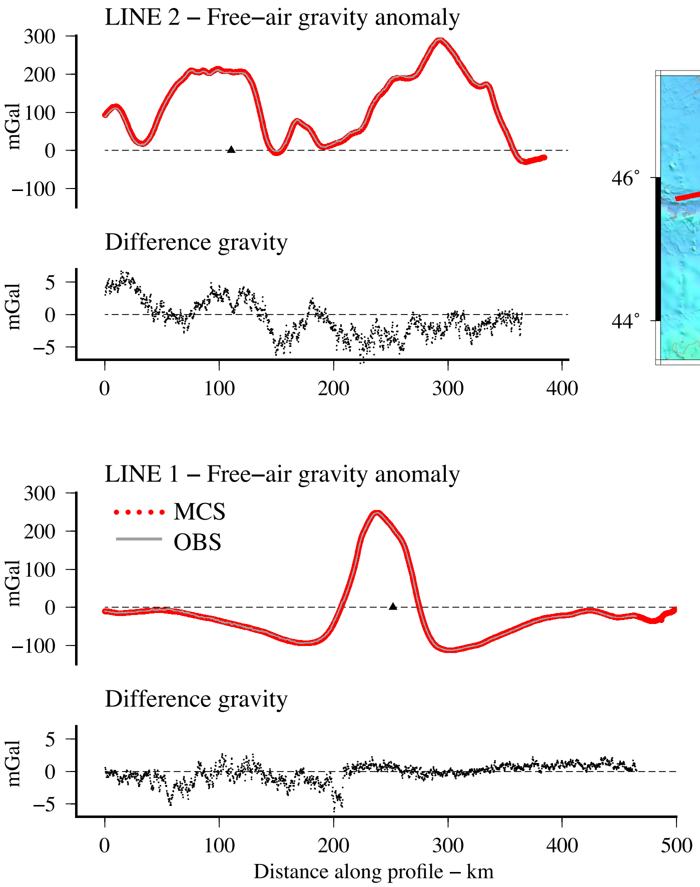

Figure 4. Comparison of free-air gravity anomaly data along repeat Lines 1 and 2 of Jimmu and Suiko seamounts. The raw BGM-3 1 s data have been filtered with a 120 s Gaussian filter before correction for latitude and Eötvös and a 1.0 km median filter after correction (Figure 2a). Black filled triangle marks the intersection of Lines 1 and 2. The difference plots show the gravity data acquired during MCS acquisition minus the gravity data acquired during OBS acquisition.

geological and geophysical data suggest the seamounts are volcanic in origin and formed on or near a mid-ocean ridge during the Late Cretaceous (Clague & Dalrymple, 1975; Watts et al., 2006), possibly from the interaction of a hotspot (Euterpe, now extinct) with a spreading ridge that separated the Pacific and Farallon plates (Kopp et al., 2003).

During MGL1902 we crossed the southwestern flank of Chopin Seamount along a track located approximately parallel to and mid-way between two previous swath bathymetry tracks. Figure 5 shows the ship track in comparison to the existing single beam PDR and multibeam swath bathymetry data and a combined bathymetry 100 × 100 m grid of the seamount based on the MGL1902 swath and SRTM15 + V2.0 (Tozer et al., 2019) satellite-derived bathymetry data.

Figure 6 compares the observed shipboard bathymetry and gravity data to the GEBCO 2019 and SRTM15 + V2.0 satellite-derived bathymetry and V28.1, DTU10, and DTU15 satellite-derived gravity data. The figure shows significant departures between the two data sets. The largest bathymetry difference (Figure 6c) occurs over the summit of the seamount where the shipboard bathymetry is deeper than the satellite-derived bathymetry by up to 250 m and shallower by up to 500 m. The largest gravity difference (Figure 6b) also occurs over the summit where the shipboard gravity anomaly exceeds the satellite-derived gravity anomaly by up to 7–12 mGal. The RMS differences in bathymetry are in the range 175.53–185.08 m, and the

Table 1
Comparison of EM122 Swath Bathymetry and BGM-3 Gravity Data Along Repeat MCS and OBS Lines 1 and 2

		N	Mean[a]	RMS	
Swath bathymetry	Line 1	1,460	−0.0036 km	0.036 km	Figure 3
Swath bathymetry	Line 2	1,860	0.190 km	0.580 km	
BGM-3 gravity	Line 1	1,860	−0.21 mGal	1.35 mGal	Figure 4
BGM-3 gravity	Line 2	1,460	−0.60 mGal	2.77 mGal	

[a] MCS acquisition minus OBS acquisition.

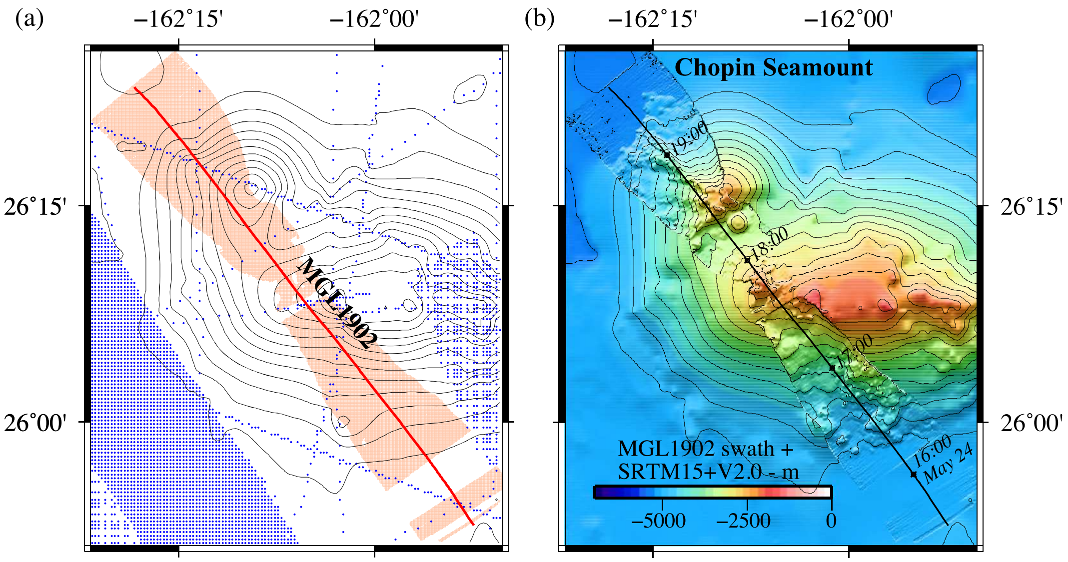

Figure 5. Surface-ship and satellite-derived bathymetry data over Chopin, Musician seamounts. (a) Previous single beam and multibeam data used to construct the SRTM15 + V2.0 model of Tozer et al. (2019). Solid red line: MGL1902 ship track. Light brown: MGL1902 swath coverage. (b) Bathymetry map based on a combined auto and manually processed swath bathymetry and SRTM15 + V2.0 100 × 100 m grid. Solid black line shows ship track with tick marks at 1 h intervals.

RMS differences in gravity are in the range 5.09–6.29 mGal (Table 2). We note that the RMS difference between the shipboard and V28.1 satellite-derived gravity field (5.09 mGal) is significantly larger than the RMS error in this field (0.33 mGal) along the profile (Sandwell et al., 2019). Therefore errors in the V28.1 field do not change the relationship observed between the bathymetry and gravity differences in Figures 6b and 6c.

The comparisons in Figure 6 suggest that while the satellite-derived data predict well the long wavelength features of the seamount, it fails to resolve the short wavelength bathymetry of its summit and flanks and their associated gravity anomalies. This is not entirely unexpected. The summits of Chopin are narrow (~5–7 km in diameter), and the design of the downward continuation stabilization filter used when generating the SRTM15 + V2.0 predicted bathymetry (Tozer et al., 2019) has a cutoff wavelength of ~10.5 at 2 km water depth, such that the summits are below the currently achievable resolution. Furthermore, satellite-derived gravity is limited by the wavelength band resolvable using satellite altimetry, which is reported ~20 km (Sandwell et al., 2019), and so does not include shorter wavelength variations in gravity such as those over the summits of Chopin that can only be recovered by shipboard data.

The correlation between the bathymetry and gravity differences in Figures 6b and 6c is close, suggesting a causative relationship. To test this, we used the fast Fourier transform (FFT) method of Parker (1972) to compute the three-dimensional gravity effect of the combined swath and satellite-derived bathymetry, sampled it along the MGL1902 ship track and compared it to the observed free-air gravity anomaly. We assumed in the calculations a density of water of 1,030 kg m^{-3}, uniform densities of bathymetry of 2,450, 2,650, and 2,850 kg m^{-3} and that the bathymetry is isostatically uncompensated. Figure 6a shows a good general agreement between the observed and calculated gravity anomalies. However, a density of 2,850 kg m^{-3} overpredicts the amplitude of the observed free-air gravity anomaly while a density of 2,450 kg m^{-3} underpredicts it. The best overall fit over the seamount summit is for a density of 2,650 kg m^{-3}, although none of the uniform densities tested is able to fully explain the gravity anomaly over both the summit and its flanks.

The differences between the observed and calculated gravity anomaly and the V28.1 and DTU15 satellite-derived gravity fields are highlighted at an expanded vertical scale in Figure 6b. Thin black dashed lines show the differences between the calculated gravity effect of the bathymetry assuming a uniform

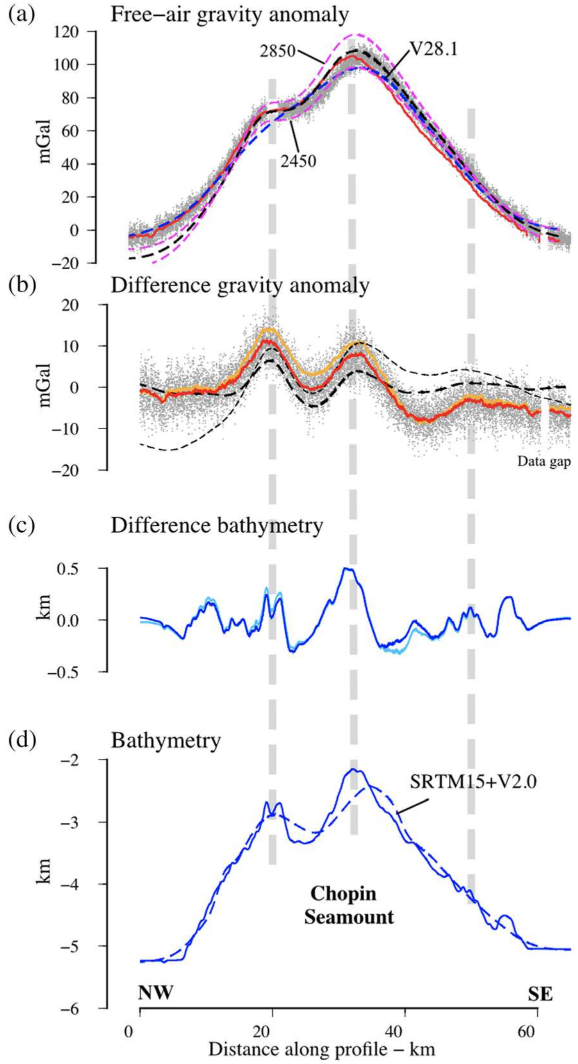

Figure 6. Comparison of shipboard bathymetry and gravity data and satellite-derived data over the west flank of Chopin, Musician Seamounts. (a) Comparison of observed 1 s data with 120 s Gaussian filter (gray filled circles) and 1 s data with 120 s Gaussian filter and a 1.0 km Gaussian filter (red solid line) with the satellite-derived V28.1 gravity field (Sandwell et al., 2019) (blue dashed line). Dashed purple lines show the three-dimensional calculated gravity effect of uncompensated bathymetry assuming a combined swath and satellite-derived bathymetry grid and uniform densities of 2,450 and 2,850 kg m^{-3}. The dashed black line shows the calculated gravity for a uniform density of 2,650 kg m^{-3}. (b) Observed BGM-3 minus satellite-derived gravity. Gray filled circles show observed 1 s data with 120 s Gaussian filter minus the V28.1 field. Red solid line shows observed with a 1.0 km median filter minus the V28.1 field. Orange solid line shows observed with a 1.0 km median filter minus the DTU15 field (Andersen et al., 2017). Thin dashed black line shows the calculated gravity effect of the combined swath and satellite-derived bathymetry based on an assumed density of 2,650 kg m^{-3} minus the V28.1 field. Thick dashed line shows a 25.0 km Gaussian filtered calculated gravity effect minus the V28.1 field. (c) Observed swath minus the satellite-derived bathymetry. Solid blue line shows SRTM15 + V2.0 (Tozer et al., 2019). Solid light blue line shows GEBCO 2019. (d) Comparison of observed 10 s center beam swath bathymetry with a 1.0 km Gaussian filter (solid blue line) to the satellite-derived SRTM15 + V2.0 bathymetry (dashed blue line).

density of 2,650 kg m^{-3} and the satellite-derived gravity fields. Thick black dashed lines shows a 25 km Gaussian filter of the difference. The filter removes the regional (down-north/up-south) tilt in the difference gravity anomaly, which we speculate, is due, at least in part, to lateral changes in density beneath the flanks of the seamount with the northern flank underlain by relatively low density crust and the southern flank by relatively high density crust. Such density differences may be reflected in the morphology of the seamount where the steeper northern flank of Chopin is more prone to submarine landsliding and mass wasting products in the form of slides and large blocks (visible in Figure 5b) than the southern flank.

5.2. Jimmu and Suiko Guyots, Emperor Seamounts

The Jimmu and Suiko guyots are two of a number seamounts that comprise the hotspot generated Hawaiian-Emperor seamount chain. Many of the seamounts have flat tops and were identified by Hess (1946), Dietz (1954), and Smoot (1982) as guyots: ancient islands that were wave-trimmed and then submerged. Jimmu and Suiko are unusually large compared to other known Pacific guyots, having an areal extent in excess of ~1,500 km^2 and rising more than 4 km above the regional depth of the surrounding seafloor. Rock dredge and IODP drilling data indicate an age for the main phase of volcano shield-building on Suiko of 60–65 Ma (Dalrymple et al., 1980) and a linear age-distance relation of 57 ± 2 km Myr^{-1} indicate a most probable age for Jimmu of 64–69 Ma (O'Connor et al., 2013).

We crossed Suiko and Jimmu guyots during MGL1902 on a ship track that connected the two summits and intersected four tracks of previous swath bathymetry cruises, including SONNE cruise SO201. Figure 7 shows the ship track in comparison to existing single beam echo sounder and multibeam swath bathymetry data and a combined bathymetry 100 × 100 m grid of the seamounts based on MGL1902 swath and SRTM15 + V2.0 satellite-derived bathymetry data.

Figure 8 compares the observed shipboard bathymetry and gravity data to satellite-derived bathymetry and gravity data. The largest bathymetry differences occur over the steep flanks of the guyots where the shipboard bathymetry is deeper than the satellite-derived bathymetry by up to 1.6 km (Figure 8c). The largest gravity differences occur over the summits of Jimmu and Suiko where the shipboard gravity anomaly is greater than the satellite-derived gravity by up to 8 mGal and over the southern flank of Suiko and northern flank of Jimmu where the shipboard gravity is smaller than the satellite-derived gravity by up to 8 mGal. The RMS difference for the SRTM15 + V2.0 bathymetry is 303.39 m and for the V28.1, DTU10, and DTU15 gravity are 2.58, 4.46, and 3.45 mGal respectively (Table 2).

The observed free-air gravity anomaly along the ship track in Figure 7 is compared to the calculated three-dimensional gravity effect of the bathymetry based on the FFT method of Parker (1972), a combined swath and satellite-derived 25 × 25 m grid and uniform densities of bathymetry of 2,200, 2,600, and 3,000 kg m^{-3} in Figure 8. Figure 8b shows that unlike at Chopin Seamount a significant discrepancy (up to 100 mGal) now exists between the observed and calculated gravity anomaly based on the bathymetry. The largest discrepancies

Table 2
Comparison of EM122 Swath Bathymetry With SRTM15 + V2.0 and GEBCO 2019 Bathymetry and BGM-3 Gravity With V28.1 and DTU10 and DTU15 Gravity

	N	Mean[a]	RMS	
Chopin				
GEBCO 2019	1,423	−3.16 m	185.08 m	Figure 6
SRTM15 + V2.0	1,423	−0.52 m	175.53 m	
V28.1	14,631	−1.11 mGal	5.09 mGal	
DTU10	14,631	−0.49 mGal	6.29 mGal	
DTU15	14,631	+0.45 mGal	5.89 mGal	
Emperor Seamounts				
GEBCO 2019	18,034	−50.01 m	244.37 m	Figure 8
SRTM15 + V2.0	18,034	−100.13 m	303.39 m	
V28.1	180,720	−1.52 mGal	2.58 mGal	
DTU10	180,720	+0.33 mGal	4.46 mGal	
DTU15	180,720	+0.14 mGal	3.45 mGal	

[a] Shipboard minus satellite-derived.

are found over the guyot summits where none of the uniform densities of the bathymetry tested are able to account for the amplitude of the observed gravity anomalies.

We assumed in the calculations in Figure 8a that the guyots are uncompensated and so have ignored any contribution to the calculated gravity anomaly in Figure 8a of a crustal "root" due, for example, to volcano load-induced flexure. A crustal "root" beneath Jimmu and Suiko would, however, reduce the amplitude of the calculated gravity anomalies and further increase the discrepancy between observed and calculated gravity anomaly. These considerations suggest that a single density contrast at the seafloor interface is insufficient to explain the observed gravity anomaly and hence other contributions due, for example, to sub-seafloor interfaces, must be involved.

In order to examine the relationship between the short wavelength bathymetry and gravity along the ship track at Jimmu and Suiko we followed the procedure used at Chopin, Musician Seamounts. The V28.1 and DTU15 satellite-derived fields were subtracted from the calculated gravity anomaly for a particular uniform density (in this case 2,600 kg m^{-3}) and the difference calculated. The difference was then filtered and another difference calculated by subtracting the filtered gravity from the unfiltered gravity. In the case of Chopin, this procedure removed a regional tilt (down-north/up-south) which we tentatively attributed to lateral changes in the density of the crust between the north and south flanks of the seamount. At Suiko and Jimmu, the difference gravity anomaly is largest over the seamount summit, and so we attribute it to lateral density changes within the respective volcano edifices. The difference implies a mass excess, suggesting the seamounts are cored by mafic material that progressively increases its density with depth. Irrespective of the actual cause, filtering removes this contribution and allows us to proceed with examining the relationship between the short wavelength bathymetry and gravity anomaly.

Figure 8c shows the observed and calculated difference gravity. The observed gravity is based on the raw 1 s shipboard data with a 120 s Gaussian filter and an additional 1.0 km de-spiking median filter. The calculated gravity is based on Gaussian filters of width 15, 25, and 35 km. The figure shows a close visual correlation between the observed gravity along the profile and the calculated gravity based on the bathymetry. The best overall fits to the amplitude and wavelength of the observed gravity are for a calculated difference gravity with a 25 km Gaussian filter, but each filter tested confirms that short wavelength variations in the BGM-3 raw 1 s data are related to changes in bathymetry, rather than to other factors such as navigation, sensor, or oceanographic "noise."

We have considered in these comparisons for Chopin seamount and Jimmu and Suiko guyots the GEBCO 2019 and SRTM15 + V2.0 satellite-derived bathymetry and the V28.1 and DTU satellite-derived gravity fields. As Figures 6 and 8 demonstrate, each of these satellite-derived fields define well Earth's bathymetry and gravity fields. However, Table 2 shows that SRTM15 + V2.0 bathymetry, which is essentially identical to GEBCO 2020, explains the shipboard bathymetry equally well as GEBCO 2019 while V28.1 gravity explains the shipboard gravity better than DTU10 and DTU15. We have therefore used the SRTM15 + V2.0 and V28.1 satellite-derived fields as the "reference" in our subsequent studies.

6. Discussion

The comparison between observed and calculated gravity at Chopin Seamount and Jimmu and Suiko guyots demonstrates not only the utility of shipboard gravity measurements in improving the resolution of the marine gravity field, but the possibility of using shipboard gravity data to constrain the density (and hence composition) of small-scale features on the seafloor. We illustrate this here by a detailed comparison of the difference between the observed and calculated gravity anomalies and the satellite-derived field over three segments of the MGL1902 ship track that crossed the summits of the Jimmu and Suiko guyots and the deep water region between them.

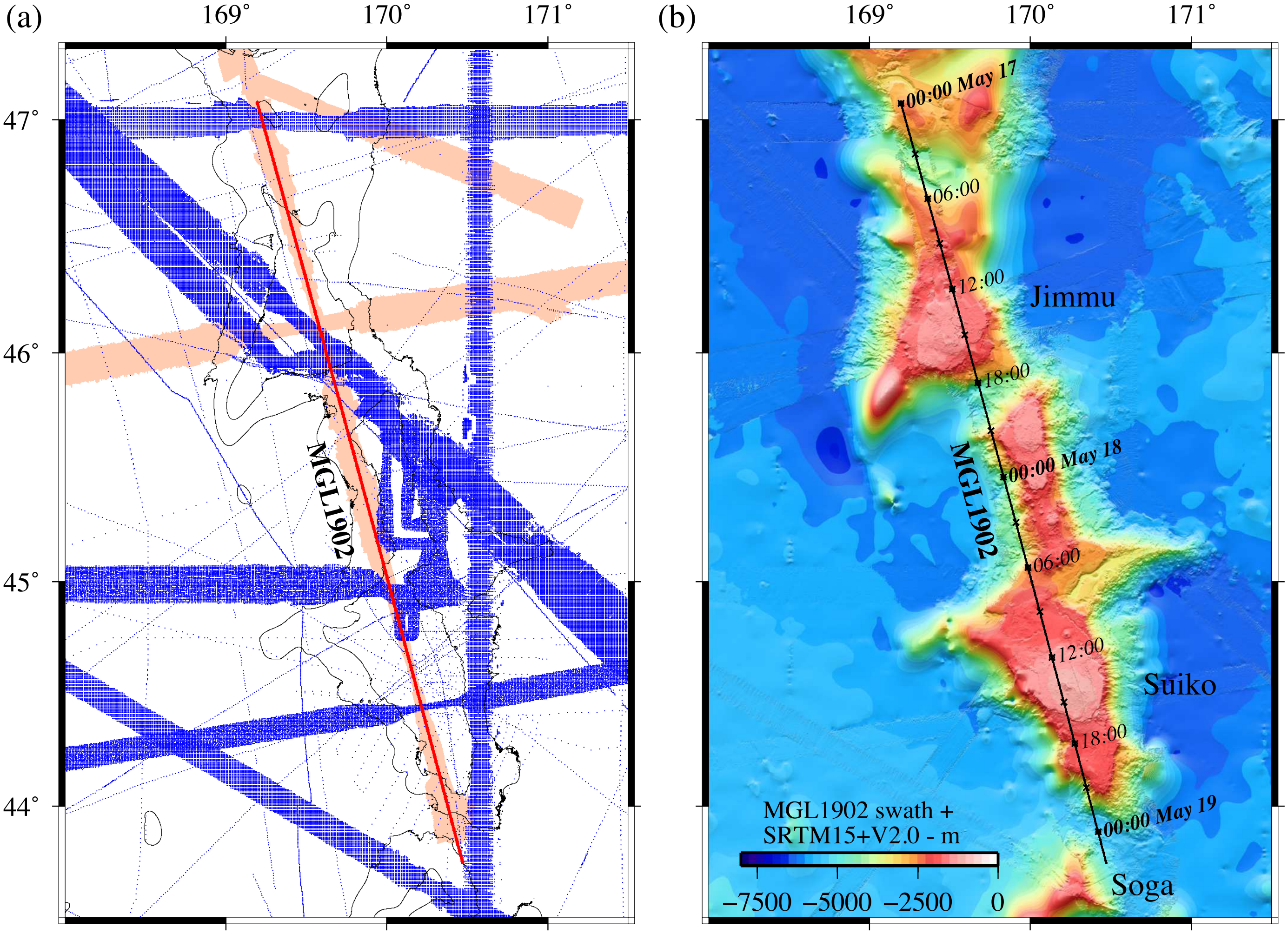

Figure 7. Surface-ship and satellite-derived bathymetry data over Jimmu and Suiko, Emperor Seamounts. (a) Previous single beam and multibeam data distribution used to construct the SRTM15 + V2.0 model (Tozer et al., 2019). Solid red line: MGL1902 ship track. Light brown: MGL1902 swath coverage.
(b) Bathymetry map based on a combined MGL1902 swath bathymetry and SRTM15 + V2.0 100 × 100 m grid. Solid black line shows tick marks at 6 hr intervals along the ship track.

Figure 9 compares observed and calculated gravity anomalies over the north flank of Jimmu. The figure shows three 6- to 10-km wide, 500-m-high, bathymetric features at depths of 1.4–1.7 km on the north-dipping flank of the guyot. The bathymetric features, labeled A, B, and C in Figure 9c, correlate with gravity anomaly highs of up to 4–6 mGal. Figures 9a and 9b compare the raw 1 s BGM-3 gravity data with a Gaussian filter of 120 s and a 1 km de-spike median filter to calculated gravity anomalies based on the FFT method of Parker (1972), a 25 × 25 m combined swath bathymetry and satellite-derived bathymetry grid and uniform densities of bathymetry of 2,200, 2,600, and 3,000 kg m^{-3}. The figures show that while there is no single uniform seabed density that can explain the observed gravity data, there are segments of the calculated gravity anomaly profiles that do appear to fit the observed data. For example, the "skewness" of the gravity effect of feature A and the relatively low amplitude of feature B appear to be best explained by a low density seafloor while the steep slope and high amplitude of feature C appear to be best explained by a high density. Figure 9d shows that features A and B appear as circular-shaped "mounds" on the seafloor, possibly volcanic cones with, at least in the case of A, a summit pit crater. The low density, if they are volcanic in origin, implies they comprise ash and, because they are in-tact, they might be significantly younger in age than the main guyot edifice. Interestingly, evidence for post-shield building volcanic activity has been proposed at Detroit Seamount, ~600 km north of Jimmu, on the basis of ash horizons in ODP drill sites which may be as much as 42 Myr younger than the volcano edifice (Kerr et al., 2005).

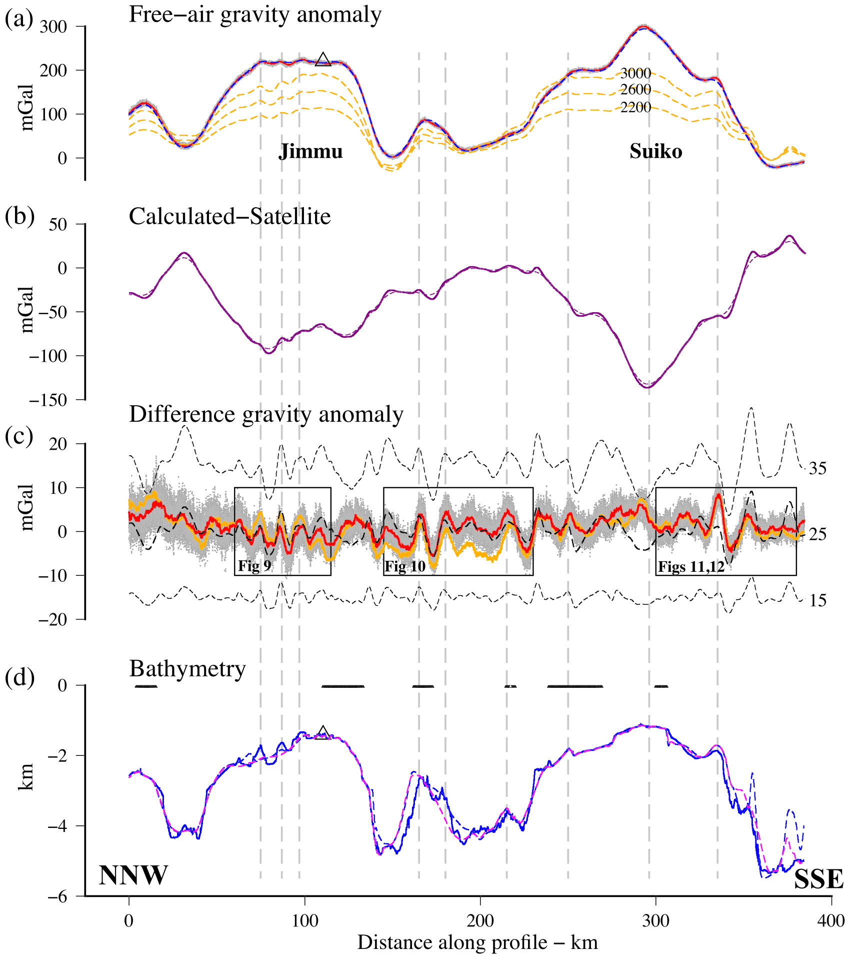

Figure 8. Comparison of observed and calculated gravity anomaly for different assumed average densities of bathymetry. (a) Observed and calculated gravity. Gray filled circles show BGM-3 raw 1 s data with 120 s Gaussian filter. Solid red line shows raw 1 s data with 120 s Gaussian filter and a 0.1 km despike median filter. Blue dashed line shows the satellite-derived V28.1 field. Dashed orange lines show the calculated three-dimensional gravity effect of the topography based on the FFT method of Parker (1972) assuming a uniform density of water of 1,030 and crust of 2,200, 2,600, and 3,000 kg m^{-3}. (b) Calculated gravity effect of the topography based on uniform density of crust of 2,650 kg m^{-3} minus the V28.1 satellite-derived gravity field. Dashed line shows the difference with a 25 km Gaussian filter. (c) Observed BGM-3 minus satellite-derived gravity. Gray filled circles show observed 1 s data with 120 s Gaussian filter minus the V28.1 field. Red solid line shows observed with a 1.0 km median filter minus the V28.1 field. Orange solid line shows observed with a 1.0 km median filter minus the DTU15 field. Thick dashed black line shows the calculated gravity for an assumed density of bathymetry of 2,650 kg m^{-3} and a 25 km Gaussian filter. Thin dashed lines, which have been shifted vertically for clarity of display, are for a 15 and 35 km Gaussian filter. Boxes locate the expanded plots in Figures 9–11. (d) Observed 10 s center beam swath bathymetry data with a 0.1 km despike median filter (solid blue line) and satellite-derived bathymetry SRTM15 + V2.0 (dashed blue line) and GEBCO 2019 (dashed magenta line). Thick black lines at zero bathymetry show the region of intersection along Line 2 of legacy swath bathymetry cruises (Figure 7a).

Feature C, in contrast, appears to be part of an incised wave-cut platform, the shoreline to which is well defined on swath bathymetry as the 1,500 m depth contour. The high density associated with this feature suggests that the platform has been incised in mafic or possibly ultramafic rocks.

Figure 10 compares observed and calculated gravity over the deep water between Jimmu and Suiko. The figure shows three similar size bathymetric features to those on Jimmu (5–15 km wide, 500 m high), but at the significantly greater depth compared to the flanks of Jimmu and Suiko of 2.6–3.5 km. The features, labeled D, E, and F in Figure 10c, correlate with gravity anomaly highs of up to 5–10 mGal. Figures 10a and 10b

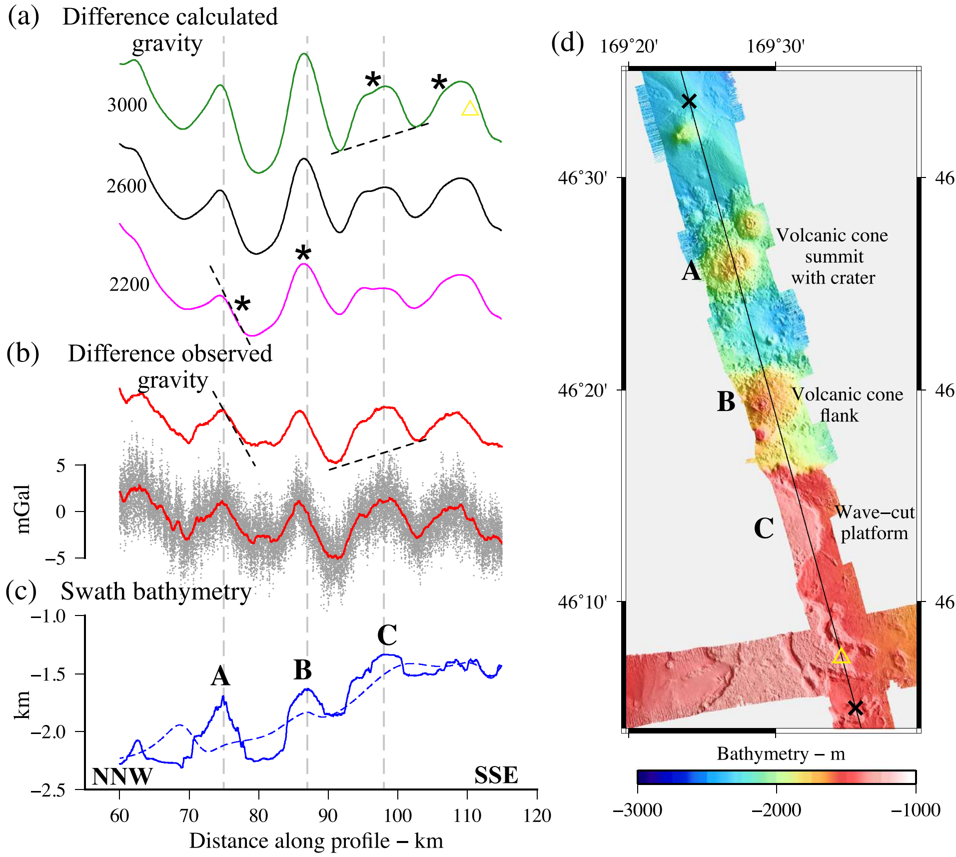

Figure 9. Comparison of the difference between observed and satellite-derived gravity and the difference between calculated and satellite-derived gravity over the north flank of Jimmu guyot. (a) Calculated gravity effect of the topography assuming three-dimensionality and uniform densities of the bathymetry of 2,200, 2,600, and 3,000 kg m^{-3} minus the V28.1 satellite-derived gravity field. The thin dashed line and asterisks indicate segments of the calculated gravity anomaly that most closely resemble the observed gravity. (b) Observed BGM-3 minus satellite-derived gravity. Gray filled circles show 1 s data with a 120 s Gaussian filter. Red lines show a 1 km (lower curve) and a 2 km (upper curve) de-spike median filter. (c) Observed 10 s center beam swath bathymetry data with a 0.1 km despike median filter (solid blue line) and satellite-derived bathymetry SRTM15 + V2.0 (dashed blue line). A, B, and C identify prominent bathymetric features discussed in the text. d) 25 × 25 m swath bathymetry grid used along with the satellite-derived bathymetry to calculate the gravity effect of the bathymetry. A, B, and C locate the bathymetric features in (c) and summarize their geological interpretation. Yellow open triangle indicates the intersection with Line 1.

compare the raw 1 s BGM-3 gravity data with a Gaussian filter of 120 s and a 1 km de-spike median filter to calculated gravity anomalies based on the FFT method of Parker (1972), a 25 × 25 m combined swath and satellite-derived bathymetry grid and assumed uniform densities of bathymetry of 2,200, 2,600, and 3,000 kg m^{-3}. The figure shows that as in the case of the Jimmu profile in Figure 9 there is no single uniform density of bathymetry that can fully explain the observed gravity data. There are, however, segments of the calculated gravity anomaly profiles that do fit the observed data. For example, features D and E appear to require an intermediate and high density in order to explain the amplitude of the observed anomaly over D and the "skewness" of the anomaly over E, while a low density appears to be required to explain the "skewness" of the anomaly over feature F. Figure 10d shows that features D and E occur in a region of what appear to be lava flow fronts on the west flank of a narrow ridge that extends NNE of Suiko guyot, consistent with mafic and maybe ultramafic rocks and an intermediate and high density.

Feature F, in contrast, appears to be associated with a region of incised channels. The channels may act as conduits that transport sediments from a region of scour upslope to a region of deposition downslope. Evidence for scour is the "scalloping" of bathymetric contours upslope of the channels and for deposition

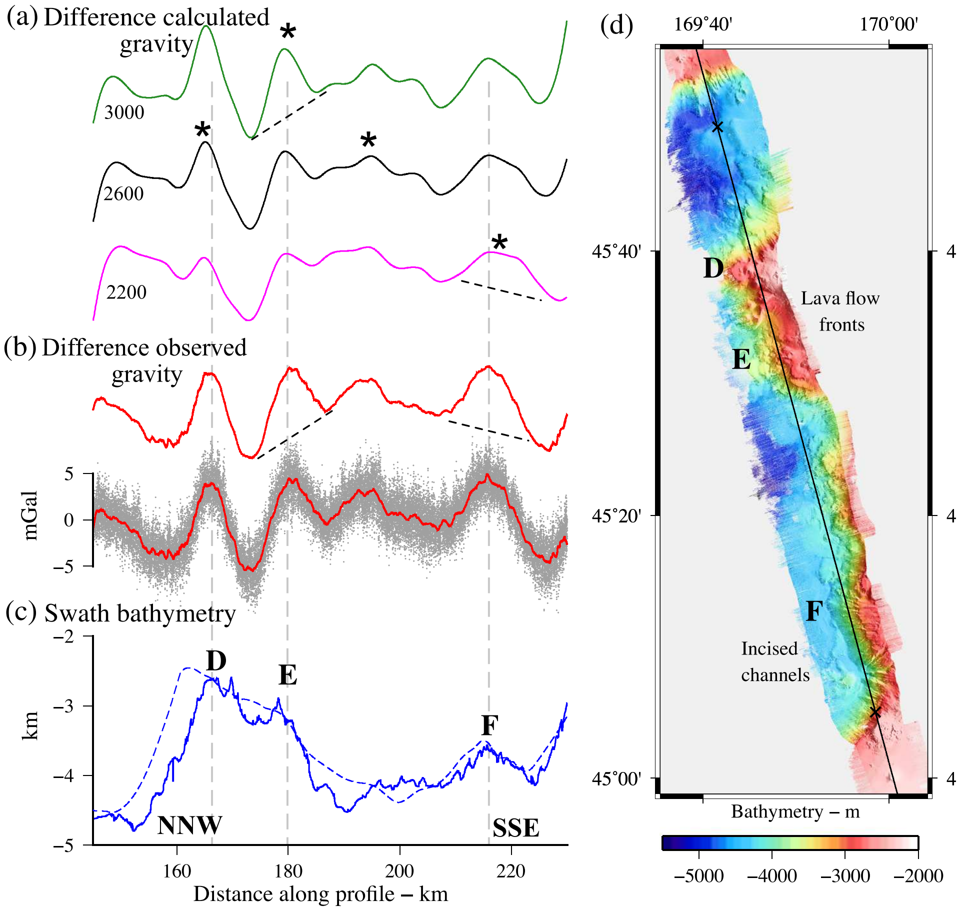

Figure 10. Comparison of the difference between observed and satellite-derived gravity and the difference between calculated gravity and satellite-derived gravity over the deep water between Jimmu and Suiko guyots. (a) Difference calculated gravity assuming three-dimensionality and uniform densities of the bathymetry of 2,200, 2,600, and 3,000 kg m^{-3}. The thin dashed line and asterisks indicate segments of the calculated gravity that most closely resemble the observed gravity. (b) Difference observed gravity. Red lines show a 1 km (lower curve) and a 2 km (upper curve) de-spike median filter. (c) Observed 10 s center beam swath bathymetry data with a 0.1 km despike median filter (solid blue line) and satellite-derived bathymetry SRTM15 + V2.0 (dashed blue line). D, E, and F identify prominent bathymetric features discussed in the text. (d) 25 × 25 m swath bathymetry grid used along with the satellite-derived bathymetry to calculate the gravity effect of the bathymetry. D, E, and F locate the bathymetric features in (c) and summarize their geological interpretation.

is the bulging of the contours downslope. The presence of mass wasting products is consistent with a low density of the bathymetry.

Figure 11 compares observed and calculated gravity anomalies over the south flank of Suiko. The figure shows three 10- to 15-km-wide, up to 750-m high, bathymetric features at depths 1.5–3.4 km on the south-dipping flank of the guyot. The bathymetric features, labeled G, H, and I in Figure 11c, correlate with gravity anomaly highs of up to 2–10 mGal. Figures 11a and 11b compare the raw 1 s BGM-3 gravity data with a Gaussian filter of 120 s and a 1 and 2 km de-spike median filter to calculated gravity anomalies based on the FFT method of Parker (1972), a 25 × 25 m combined swath bathymetry and satellite-derived bathymetry grid and uniform densities of bathymetry of 2,200, 2,600, and 3,000 kg m^{-3}. The figure again shows that while there is no single uniform density of bathymetry that can explain the observed gravity data, there are segments of the calculated gravity anomaly profiles that do appear to fit the observed data. For example, feature G is a gentle upwarp of the seafloor and appears to require an intermediate density to explain the amplitude and "skewness" of the associated gravity anomaly high while feature I is a mid-slope bathymetric high which

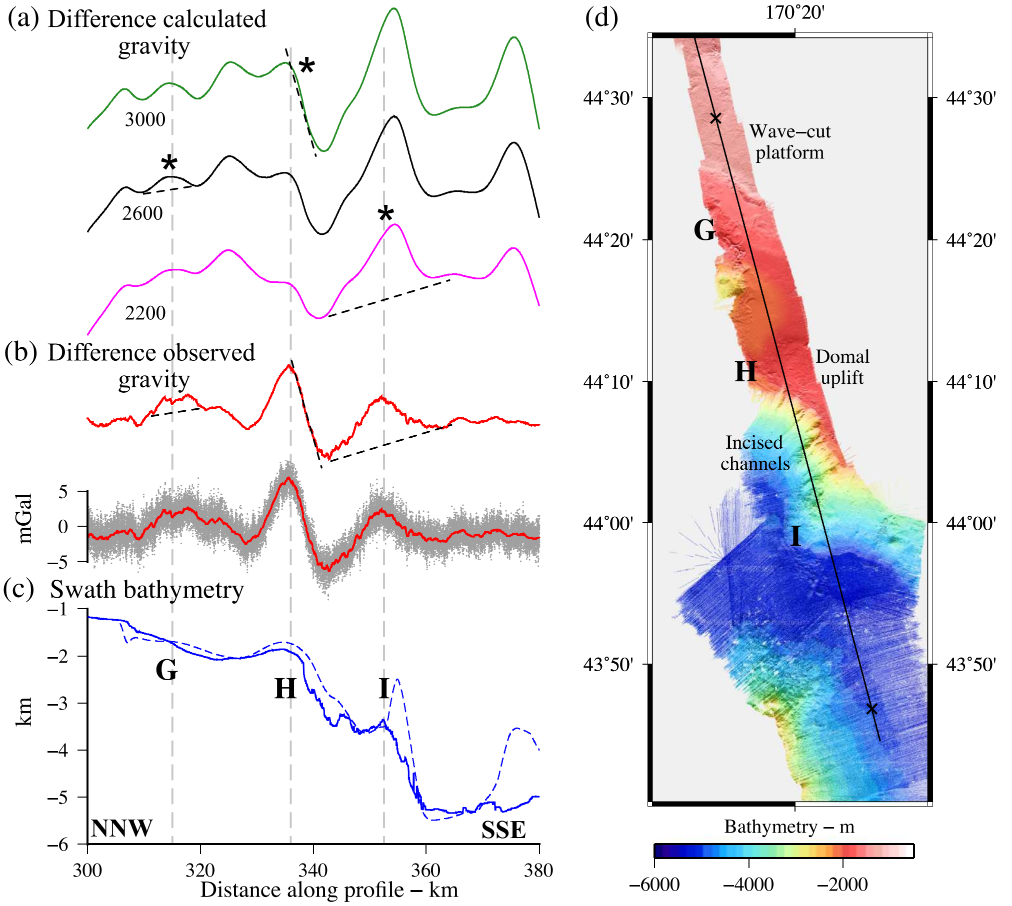

Figure 11. Comparison of the difference between observed and satellite-derived gravity and the difference between calculated gravity and satellite-derived gravity over the south flank of Suiko guyot. (a) Difference calculated gravity assuming three-dimensionality and uniform densities of the bathymetry of 2,200, 2,600, and 3,000 kg m^{-3}. The thin dashed line and asterisks indicate segments of the calculated gravity that most closely resemble the observed gravity. (b) Difference observed gravity. Red lines show a 1 km (lower curve) and a 2 km (upper curve) de-spike median filter. (c) Observed 10 s center beam swath bathymetry data with a 0.1-km despike median filter (solid blue line) and satellite-derived bathymetry SRTM15 + V2.0 (dashed blue line). G, H, and I identify prominent bathymetric features discussed in the text. (d) 25 × 25 m swath bathymetry grid used along with the satellite-derived bathymetry to calculate the gravity effect of the bathymetry. G, H, and I locate the bathymetric features in (c) and summarize their geological interpretation.

appears to require a low density to explain the associated gravity high. Figure 11d shows that feature G is downslope of what appears to be a wave-cut platform on smooth seafloor, consistent with mafic rocks while feature I is located just to the south of incised channels and north of a region of what appear to be blocks scattered over a broad region of deep seafloor, consistent with erosional scour, sediment transport, and deposition.

Feature H, however, is enigmatic. The swath bathymetry map (Figure 11d) reveals a broad domal uplift of the seafloor, yet the calculated gravity anomaly predicts a significantly smaller gravity anomaly high over this feature than is observed. Nevertheless, there is a suggestion from the steep gravity anomaly gradient associated with the south flank of feature H that high density rocks may be present. We speculate therefore that feature H is an igneous complex comprising mafic and/or ultramafic rocks that have intruded the host rocks in such a way to elevate the uppermost crustal layers and the seafloor. Similar intrusive complexes have been deduced by Flinders et al. (2013) using difference gravity anomalies in the Hawaiian Islands region.

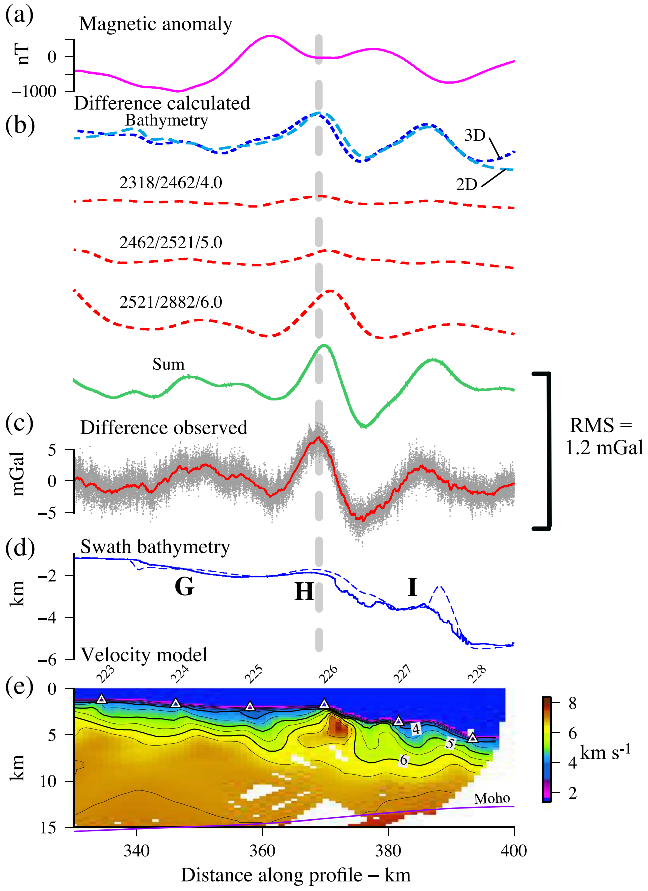

Figure 12. Comparison of the bathymetry and gravity anomaly features on the south flank of Suiko to seismic *P* wave velocity structure and magnetic anomaly data. The *P* wave velocity structure is based on Grevemeyer et al. (2019), and magnetic anomaly data were acquired during MGL1902. (a) Magnetic anomaly. (b) Difference calculated gravity obtained by subtracting the V28.1 satellite-derived gravity field from the calculated gravity effect of the bathymetry and the seismically constrained crustal model. Blue dashed lines show the two-dimensional gravity effect of the bathymetry based on the 10 s swath center beam data (light blue) and the three-dimensional gravity effect of the bathymetry based on a 25 × 25 m swath grid (dark blue). Red dashed lines show the gravity effect of the crustal layers as defined by the depth to the 4.0, 5.0, and 6.0 km s^{-1} isovelocity contours and the velocity-density relationships of Brocher (2005). Numbers indicate the density in kg m^{-3} above, the density below in kg m^{-3}, and the isovelocity contour in km s^{-1} across which the density contrast between the two layers is assumed to apply. Green solid line shows the sum gravity effect of all the crustal layers. (c) Difference observed gravity anomaly. Gray filled circles show 1 s data with a 120 s Gaussian filter. Red lines show a 1 km de-spike median filter. (d) 25 × 25 m swath bathymetry grid used along with the satellite-derived bathymetry. G, H, and I locate the bathymetric features in Figure 11. (e) Crustal *P* wave velocity model derived by Grevemeyer et al. (2019) based on OBS data acquired along Line 2 during MGL1902. Thick black lines show the 4.0, 5.0, and 6.0 km s^{-1} isovelocity contours, the two-dimensional gravity effect of which are shown in (b).

To further test this possibility, we compared the bathymetry and gravity data in the region of feature H on the south flank of Suiko to other available marine geophysical data (Figure 12). The figure shows that the bathymetry and gravity feature H closely correlates with high *P* wave velocities (>6 km s^{-1}) (Grevemeyer et al., 2019) and a broad magnetic anomaly "high" (~400–600 nT), consistent with the occurrence of a mafic or ultramafic crustal body at shallow depth below the seafloor. There is an excellent agreement between the difference observed gravity based on the median filtered 1 s BGM-3 data and the difference calculated gravity based on the two-dimensional gravity effect of the crustal layers defined seismically (RMS = 1.2 mGal). While the gravity effect of the bathymetry is still a significant contributor to the gravity anomaly, Figure 12b clearly shows the shallowing of the 6.0 km s^{-1} iso-velocity contour to be equally significant. We believe this result is robust, despite the fact that the gravity effects of the crustal layers have been computed assuming the line-integral method of Talwani et al. (1959) rather than the FFT method of Parker (1972) and two- rather than three-dimensionality. The figure shows, for example, that in the case of the gravity effect of the bathymetry, the difference between assuming two- and three-dimensionality (blue dashed lines in Figure 12b) is small and does not exceed a RMS of 0.8 mGal.

7. Conclusions

1. A recent survey of Chopin seamount and Jimmu and Suiko guyots in the northwest Pacific Ocean reveals RMS differences between shipboard measurements and satellite-derived bathymetry and gravity data in the range 175.5–303.4 m and 2.6–6.3 mGal, respectively.
2. The differences reflect the high-resolution of current shipboard swath bathymetry and gravity measurement systems, such as those installed on R/V *Marcus G. Langseth*, and the lower resolution of global satellite-derived bathymetry and gravity due to limits in the technique of bathymetric prediction and the wavelengths resolvable using satellite altimetry.
3. The bathymetry and gravity differences are, in many cases, highly correlated and can be explained to a significant degree by the gravity effect of uncompensated bathymetry with densities that are in the range 2,200–3,000 kg m^{-3}, suggesting significant variation in rock type on the seafloor.
4. Shipboard systems such as the Koninsberg EM 120 swath bathymetry and BGM-3 gravimeter are capable of resolving seafloor features as small as 5–15 km wide and 250–500 m high, even in water depths of 2–4 km.
5. These features in the shipboard bathymetry and free-air gravity anomaly field are unresolvable in current global satellite-derived solutions such as GEBCO 2019 and SRTM15 + V2.0 and DTU10, DTU15 and V28.1.
6. Surface ship swath bathymetry and gravity measurements will continue to be required in the future, not only for global Earth model improvement, but also for marine geological studies, especially those involved with the structure and composition of seamounts, the processes contributing to their growth and decay, and their significance for intraplate volcanism.

Appendix A: BGM-3 Gravimeter tie-in Data

Following the installation of a new sensor during 11–15 June 2018 in Honolulu the BGM-3 gravimeter onboard R/V *Marcus G. Langseth* was set to a digital pulse rate conversion factor and bias of 5.096606269 mGal/count and 852,513.49 mGal, respectively. Since its installation the sensor has drifted (Figure A1) resulting in a mistie at the start of MGL1902 of +9.82 mGal in Honolulu, which had decreased to +6.25 mGal by the end of the cruise in Kodiak on 2 June 2019 (Figure A1). The resulting drift was −0.0744 mGal/day. The Chopin seamount gravity survey was carried out 9 days after the Honolulu tie and the Emperor Seamount gravity surveys 31–38 days after the Honolulu tie. We therefore applied a mistie correction to the Chopin and Emperor Seamount gravity data of +9.15 and +7.25 mGal, respectively.

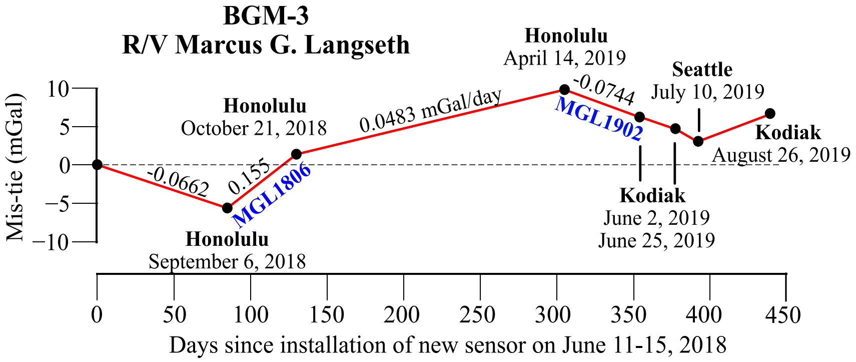

Figure A1. Misties between the observed and expected values of gravity in port for a 450-day-long period following installation of a new BGM-3 sensor in Honolulu during 11–15 June 2018.

Data Availability Statement

The figures in this paper were constructed using GMT (Wessel & Smith, 1991). The swath bathymetry, gravity, and magnetic data acquired during the MGL1902 cruise (https://doi.org/10.7284/908198) will be made available through the Marine Geoscience Data System (MGDS).

Acknowledgments

We are grateful to the officers, crew, and scientific and technical staff onboard R/V *Marcus G. Langseth* for making the acquisition of the swath bathymetry and gravity data used in this paper possible and V. Cortes Rivas, W. Fortin, H. Harper, J. Leeburn, M. Liu, and C. L. Nguyen for their help with data editing at sea. D. Sandwell (Scripp's Institution of Oceanography, USA) provided the SRTM15 + V2.0 and V28.1 global fields prior to the cruise and made a number of helpful comments on an early version of the manuscript. We thank two anonymous reviewers for their helpful comments and O. Andersen (Denmark National Space Institute) for making available the DTU15 global gravity field. This research was supported by National Science Foundation grant OCE-1737245.

References

Andersen, O. B., Knudsen, P., & Berry, P. (2010). The DNSC08GRA global marine gravity field from double retracked satellite altimetry. *Journal of Geodesy*, *84*(3), 191–199. https://doi.org/10.1007/s00190-009-0355-9

Andersen, O. E., Knudsen, P., Kenyon, S., Factor, J. K., & Holmes, S. (2017). Global gravity field from recent satellites (DTU15)—Arctic improvements. *First Break*, *35*(12). https://doi.org/10.3997/1365-2397.2017022

Bell, R. E., Anderson, R., & Pratson, L. (1997). Gravity gradiometry surfaces. *The Leading Edge*, *16*(1), 55–59. https://doi.org/10.1190/1.1437431

Bell, R. E., & Watts, A. B. (1986). Evaluation of the BGM-3 sea gravity meter system on board *R/V Conrad*. *Geophysics*, *51*, 1480–1493.

Born, G. H., Dunne, J. A., & Lame, D. B. (1979). SEASAT mission overview. *Science*, *204*(4400), 1405–1406. https://doi.org/10.1126/science.204.4400.1405

Brocher, T. M. (2005). Empirical relations between elastic wavespeeds and density in the Earth's crust. *Bulletin of the Seismological Society of America*, *95*(6), 2081–2092. https://doi.org/10.1785/0120050077

Cande, S. C., LaBrecque, J. L., Larson, R. L., Pitman, W. C., Golovchenko, X., & Haxby, W. F. (1989). Magnetic lineations of the world's ocean basins, scale 1:27,400,000, Am. Assoc. Pet. Geol, Tulsa, Oklahoma.

Caress, D. W., & Chayes, D. N. (2019). Mapping the seafloor: Software for the processing and display of swath sonar data. http://www.mbari.org/data/mbsystem/html/mbsystem_home.html

Carlson, R. L., & Raskin, G. S. (1984). The density of the ocean crust. *Nature*, *311*(5986), 555–558. https://doi.org/10.1038/311555a0

Casten, U., & Haussmann, U. (1990). Improvement of observation accuracy of the Lacoste-Romberg (model-D) gravity meter by supplementary installation of electronic feedback. *Geophysical Prospecting*, *38*(5), 489–498. https://doi.org/10.1111/j.1365-2478.1990.tb01858.x

Clague, D. A., & Dalrymple, G. B. (1975). Cretaceous K-Ar ages of volcanic rocks from the musicians seamounts and the Hawaiian ridge. *Geophysical Research Letters*, *2*(7), 305–308. https://doi.org/10.1029/GL002i007p00305

Dalrymple, G. B., Lanphere, M. A., & Clague, D. A. (1980). Conventional and ^{40}Ar/^{39}Ar K-Ar ages of volcanic rocks from Ojin (site 430), Nintoku (site 432) and Suiko (site 433) seamounts and the chronology of volcanic propagation along the Hawaiian-emperor chain. *Initial Rep. Deep Sea Drilling Project*, *55*, 659–676.

Dietz, R. S. (1954). Marine geology of Northwestern Pacific: Description of Japanese bathymetric chart 6901. *Bulletin Geological Society of America*, *65*(12), 1199–1224. https://doi.org/10.1130/0016-7606(1954)65[1199:MGONPD]2.0.CO;2

Dixon, T. H., Naraghi, M., McNutt, M. K., & Smith, S. M. (1983). Bathymetric prediction from Seasat altimeter data. *Journal of Geophysical Research*, *88*(C3), 1563–1571. https://doi.org/10.1029/JC088iC03p01563

Flinders, A. F., Ito, G., Garcia, M. O., Sinton, J. M., Kauahikaua, J., & Taylor, B. (2013). Intrusive dike complexes, cumulate cores, and the extrusive growth of Hawaiian volcanoes. *Geophysical Research Letters*, *40*, 3367–3373. https://doi.org/10.1002/grl.50633

GEBCO Compilation Group (2020). GEBCO 2020 Grid. https://doi.org/10.5285/a29c5465-b138-234d-e053-6c86abc040b9

Grevemeyer, I., Watts, A. B., Shillington, D. J., Dunn, R., Boston, B., Gomez de la Pena, L., et al. (2019). Seismic structure along the emperor seamount chain and flexural response of the lithosphere—Preliminary results from RV Marcus G. Langseth Cruise MGL1902, Abstract, 2019 AGU Fall Meeting, San Francisco.

Hess, H. H. (1946). Drowned ancient islands of the Pacific basin. *American Journal of Science*, *244*(11), 772–791. https://doi.org/10.2475/ajs.244.11.772

Hildebrand, J. A., Stevenson, J. M., Hammer, P. T. C., Zumberge, M. A., & Parker, R. L. (1990). A seafloor and sea surface gravity survey of axial volcano. *Journal of Geophysical Research*, *95*(B8), 12,751–12,763. https://doi.org/10.1029/JB095iB08p12751

Kalnins, L. M., & Watts, A. B. (2009). Spatial variations in effective elastic thickness in the western Pacific Ocean and their implications for Mesozoic volcanism. *Earth and Planetary Science Letters*, *286*(1–2), 89–100. https://doi.org/10.1016/j.epsl.2009.06.018

Kaula, W. M. (1967). Geophysical implications of satellite determinations of the Earth's gravitational field. *Space Science Reviews*, *7*(5–6), 769–794. https://doi.org/10.1007/BF00542895

Kerr, B. C., Scholl, D. W., & Klemperer, S. L. (2005). Seismic stratigraphy of Detroit seamount, Hawaiian-emperor seamount chain: Post-hot-spot shield building volcanism and deposition of the Meiji drift. *Geochemistry, Geophysics, Geosystems*, *6*, Q07L10. https://doi.org/10.1029/2004GC000705

Kopp, H., Kopp, C., Morgan, J. P., Flueh, E. R., Weinrebe, W., & Morgan, W. J. (2003). Fossil hot spot-ridge interaction in the musicians Seamount Province: Geophysical investigations of hot spot volcanism at volcanic elongated ridges. *Journal of Geophysical Research*, *108*, 2166. https://doi.org/10.1029/2002JB002015

Lerch, F. J., Marsh, J. G., Klosko, S. M., & Williamson, R. G. (1982). Gravity model improvement for SEASAT. *Journal of Geophysical Research*, *87*(C5), 3281–3296. https://doi.org/10.1029/JC087iC05p03281

Ligi, M., Bonatti, E., Bortoluzzi, G., Cipriani, A., Cocchi, L., Caratori, T., et al. (2012). Birth of an ocean in the Res Sea; Initial pangs. *Geochemistry, Geophysics, Geosystems*, *13*, Q08009. https://doi.org/10.1029/2012GC004155

Marks, K. M. (1996). Resolution of the Scripps/NOAA marine gravity field from satellite altimetry. *Geophysical Research Letters*, *23*(16), 2069–2072. https://doi.org/10.1029/96GL02059

Marks, K. M., Smith, W. H. F., & Sandwell, D. T. (2013). Significant improvements in marine gravity from ongoing satellite missions. *Marine Geophysical Researches*, *34*(2), 137–146. https://doi.org/10.1007/s11001-013-9190-8

Nettleton, L. L. (1939). Determination of density for reduction of gravity observations. *Geophysics*, *4*(3), 176–183. https://doi.org/10.1190/1.0403176

NOAA (2019). National Data Buoy Centre. https://www.ndbc.noaa.gov/

O'Connor, J. M., Steinberger, B., Regelous, M., Koppers, A. A. P., Wijbrans, J. R., Haase, K. M., et al. (2013). Constraints on past plate and mantle motion from new ages for the Hawaiian-emperor seamount chain. *Geochemistry, Geophysics, Geosystems*, *14*, 4564–4584. https://doi.org/10.1002/ggge.20267

Olson, C. J., Becker, J. J., & Sandwell, D. T. (2014). A new global bathymetry map at 15 arcsecond resolution for resolving seafloor fabric: SRTM15 PLUS, Abstract, 2014 AGU Fall Meeting, San Francisco.

Parker, R. L. (1972). The rapid calculation of potential anomalies. *Geophysical Journal of the Royal Astronomical Society*, *31*, 447–455.

Picard, K., Brooke, B., & Coffin, M. F. (2017). Geological insights from Malaysia airlines flight MH370 search. *Eos*, *98*. https://doi.org/10.1029/2017EO069015

Rapp, R. H. (1989). The decay of the spectrum of the gravitational potential and the topography for the earth. *Geophysical Journal International*, *99*(3), 449–455. https://doi.org/10.1111/j.1365-246X.1989.tb02031.x

Renard, V., & Allenou, J. P. (1979). SeaBeam multi-beam echosounding in "Jean Charcot", description, evaluation and first results. *International Hydrographic Review*, *56*, 35–67.

Sandwell, D. T., Harper, H., Tozer, B., & Smith, W. H. F. (2019). Gravity field recovery from geodetic altimeter missions. *Advances in Space Research*. https://doi.org/10.1016/j.asr.2019.09.011

Smith, W. H. F., & Sandwell, D. T. (1994). Bathymetric prediction from dense satellite altimetry and sparse shipboard bathymetry. *Journal of Geophysical Research*, *99*(B11), 21,803–21,824. https://doi.org/10.1029/94JB00988

Smith, W. H. F., & Sandwell, D. T. (1995). Marine gravity field from declassified GEOSAT and ERS1 altimetry. *Eos*, *76*, 156.

Smith, W. H. F., & Sandwell, D. T. (1997). Global Sea floor topography from satellite altimetry and ship depth soundings. *Science*, *277*(5334), 1956–1962. https://doi.org/10.1126/science.277.5334.1956

Smoot, N. C. (1982). Guyots of the mid-emperor chain mapped with multi-beam sonar. *Marine Geology*, *47*(1–2), 153–163. https://doi.org/10.1016/0025-3227(82)90024-X

Stanley, H.-R. (1979). The GEOS-3 project. *Journal of Geophysical Research*, *84*, 3861–3871.

Talwani, M., Dorman, J., Worzel, J. L., & Bryan, G. M. (1966). Navigation at sea by satellite. *Journal of Geophysical Research*, *71*(24), 5891–5902. https://doi.org/10.1029/JZ071i024p05891

Talwani, M., Worzel, J. L., & Landisman, M. (1959). Rapid gravity computations for two-dimensional bodies with applications to the Mendocino submarine fracture zones. *Journal of Geophysical Research*, *54*, 49–59.

Tozer, B., Sandwell, D. T., Smith, W. H. F., Olson, C., Beale, J. R., & Wessel, P. (2019). Global bathymetry and topography at 15 arc sec: SRTM15+. *Earth and Space Science*, *6*, 1847–1864. https://doi.org/10.1029/2019EA000658

Tsuboi, C., Tomoda, Y., & Kanamori, H. (1961). Continuous measurements of gravity on board a moving surface ship. *Proceedings. Japan Academy*, *37*(9), 571–576. https://doi.org/10.2183/pjab1945.37.571

Watts, A. B., & Moore, J. D. P. (2017). Flexural isostasy: Constraints from gravity and topography power spectra. *Journal of Geophysical Research: Solid Earth*, *122*, 8417–8430. https://doi.org/10.1002/2017JB014571

Watts, A. B., Sandwell, D. T., Smith, W. H. F., & Wessel, P. (2006). Global gravity, bathymetry, and the distribution of submarine volcanism through space and time. *Journal of Geophysical Research*, *111*, B08408. https://doi.org/10.1029/2005JB004083

Wessel, P., & Smith, W. H. F. (1991). Free software helps map and display data. *Eos Transactions American Geophysical Union*, *72*(41), 441–446. https://doi.org/10.1029/90EO00319

Widiwijayanti, C., Mikhailov, V., Diament, M., Deplus, C., Louat, R., Tikhotsky, S., & Gvishiani, A. (2003). Structure and evolution of the Molucca Sea area: Constraints based on interpretation of a combined sea-surface and satellite gravity dataset. *Earth and Planetary Science Letters*, *215*(1–2), 135–150. https://doi.org/10.1016/S0012-821X(03)00416-3

Worzel, J. L. (1959). Continuous gravity measurements with the Graf Sea gravimeter. *Journal of Geophysical Research*, *64*(9), 1299–1316. https://doi.org/10.1029/JZ064i009p01299